International Journal of Modern Physics A
Vol. 36, Nos. 11 & 12 (2021) 2140026 (23 pages)

DOI: 10.1142/S0217751X21400261

System modeling in data processing of Taiji-1 mission

Xiaodong Peng[*,†,‡], Hongbo Jin[§], Peng Xu[¶,‖,¶¶], Zhi Wang[¶,**,‖‖], Ziren Luo[†,¶,††], Xiaoshan Ma[‡], Li-E Qiang[‡], Wenlin Tang[‡], Xin Ma[‡], Yuzhu Zhang[‡], Zuolei Wang[‡‡], Pengzhan Wu[‖], Xiaoqin Deng[**], Haosi Li[§§], Liming Wu[§§], Juan Wang[††], Yuxiao Wei[§§], Zhiyong Lin[§§], Chen Gao[‡] and Mengyuan Zhao[‡]

[*] *School of Fundamental Physics and Mathematical Sciences, Hangzhou Institute for Advanced Study, UCAS, Hangzhou 310024, China*

[†] *International Centre for Theoretical Physics Asia-Pacific, Beijing/Hangzhou, China*

[‡] *National Space Science Center, Chinese Academy of Sciences, Beijing 100190, China*

[§] *National Astronomical Observatories, Chinese Academy of Sciences, Beijing 100101, China*

[¶] *Hangzhou Institute for Advanced Study, University of Chinese Academy of Sciences, Hangzhou 310024, China*

[‖] *School of Physical Science and Technology, Lanzhou University, Lanzhou 730000, China*

[**] *Changchun Insitute of Optics, Fine Mechanics and Physics, Chinese Academy of Sciences, Changchun 130033, China*

[††] *Institute of Mechanics, Chinese Academy of Sciences, Beijing 100190, China*

[‡‡] *Lanzhou Institue of Physics, Lanzhou 730000, China*

[§§] *Chang'an University, Xi'an 710054, China*

[¶¶] *xp@lzu.edu.cn*

[‖‖] *wz070611@126.com*

[1] *On behalf of The Taiji Scientific Collaboration*

Received 15 September 2020
Revised 16 October 2020
Accepted 30 October 2020
Published 9 April 2021

Taiji-1 is the first technology demonstration satellite of the Taiji Program in Space, which, served as the pre-PathFinder mission, had finished its nominal science operational phase and successfully accomplished the mission goal. The gravitational reference sensor (GRS) on-board Taiji-1 is one of the key science payloads that coupled strongly to other instruments, sub-systems and also the satellite platform itself. Fluctuations of the physical environment inside the satellite and mechanical disturbances of the platform generate important noises in the GRS measurements, therefore their science data can also

Xiaodong Peng and Hongbo Jin contributed equally to this work.
[¶¶,‖‖] Corresponding authors.
[1] For more details, please refer to article 2102002 of this Special Issue.

be used to evaluate the performance of the μN-thrusters and the stability of the platform. In this work, we report on the methods employed in Taiji-1 GRS data processing in the systematical modelings of the spacecraft orbit and attitude perturbations, mechanical disturbances, and internal environment changes. The modeled noises are then removed carefully from the GRS science data to improve the data quality and the GRS in-orbit performance estimations.

Keywords: Gravitational wave detection; gravitational reference sensor; data analysis; spacecraft modeling.

1. Introduction

Based on the preliminary studies since 2008 and also encouraged by LIGOs first detection of gravitational wave (GW) in 2015,[1,2] the "Taiji Program in Space" was officially released by the Chinese Academy of Sciences (CAS) in 2016 and had set forth on the journey to the Chinese first space-borne GW observatory, the Taiji mission, that is expected to be launched in early 2030s.[3–5] The Taiji mission was designed, since 2011,[6–11] to be a heliocentric mission, and will have three spacecrafts (SC) forming a triangular constellation with baseline about 3×10^6 km and sensitive band between 0.1 mHz and 1 Hz. When operational, the science objectives of Taiji mission will enclose sources such as coalescing super massive black hole binaries, extreme and intermediate mass ratio binary inspirals, galactic binaries, stochastic GW background and also unmodeled sources.[5,12]

The Taiji Program will follow a three step research and development (R&D) road map,[3–5,12] see Fig. 1. Started in 2018, the CAS had funded a Strategic Priority Research Program to tackle challenges in Taiji's key technologies and to carry out the first-stage ground-based tests, and most importantly to launch the first technology demonstration satellite, that the Taiji-1 mission.[13] After the first anniversary of Taiji-1, the R&D towards a full-fledged Taiji-Pathfinder mission, that the Taiji-2 mission with twin satellites, was commissioned and initiated in AUG 2020, which is expected to be launched between 2023 and 2024 and will perform the tests of most the Taiji technologies.

The Taiji-1 satellite was launched on August 31, 2019 into a circular and sun-synchronous orbit with altitude about 600 km. Now been regarded as the Pre-PathFinder of Taiji mission, Taiji-1 was designed in the first place to test the most important individual technologies concerning gravitational reference sensors (GRS), drag-free controls (DFC), laser interferometry in space, and ultra-stable and super-clean satellite platforms. The key measurement system of Taij-1 consists of the GRS installed at the mass center of the satellite and the on-board laser interferometers served also as an independent readout system of the GRS. Cold gas thrusters were used to control the spacecraft (S/C), and two different types of colloidal μN-thrusters were installed for in-orbit performance tests and to conduct the drag-free control experiments along the radial direction. Having completed its nominal science operations in the last year, Taiji-1 had confirmed and demonstrated the design performances of the scientific payloads and the stability of the satellite platform. With

the aid of drag-free controls, the measured disturbances $S_{\Delta a}^{1/2}$ between 10 mHz and 1 Hz of the single GRS on-board had reached the amplitude spectrum density (ASD) levels below $10^{-9}\mathrm{m/s^2/Hz^{1/2}}$, that well below the expected disturbances level from air drag and solar radiation perturbations at this orbital altitude. The laser interferometer showed an ASD level of measured noise better than $100\,\mathrm{pm/Hz^{1/2}}$ in the same band, which was mainly caused by small vibrations of the platform during the experiments. The modelings of such platform vibrations are explained in this work. The resolutions of the colloidal μN-thruster evaluated by the GRS was found to be $\sim 10^{-7} N$. During its science operation phase, Taiji-1 had successfully accomplished its mission goal and had verified the feasibility of the R&D road map of the Taiji Program.

Benefited from the properly designed in-orbit experiment plan that after the one year operation lasted much longer than the designed mission lifetime, the Taiji-1 satellite still remains in good condition and with adequate resources. Now, Taiji-1, in its extended phase, continues to carry out the more challenging experiments concerning the GRS and DFC with updated and further optimized working modes and algorithms. With the accumulated orbit data from the GNSS and the nonconservative forces obtained by the GRS, Taiji-1 will also provide an independent map out of the global geopotential field.

For the aforementioned experiments, especially the planned extended experiments aiming to adjust the GRS system and to improve its overall performance, the identifications and calibrations of the full dynamical system including the satellite platform coupled through the interface of the DFC loop turn out to be crucial in understanding and analyzing the measured data. In this work, we report on the methods employed by far in analyzing the Taiji-1 GRS measurements and diagnosing the payload and platform. In Sec. 2, we introduce the GRS system and the data analysis task that ran at the Taiji-1 Data Processing Center. In Sec. 3, the modeling

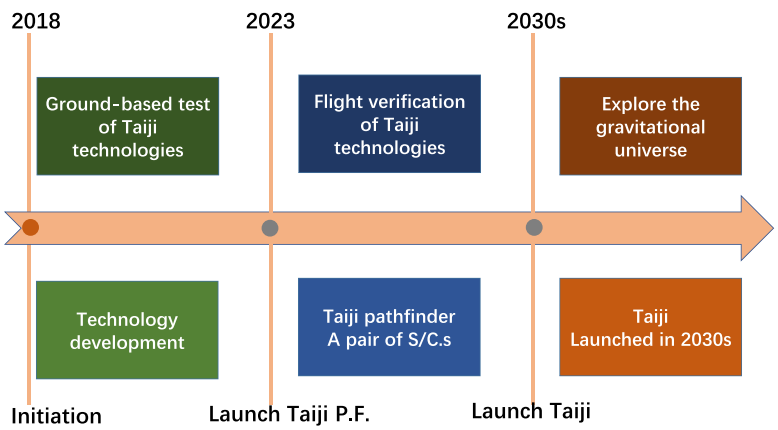

Fig. 1. The road map of the Taiji Program.

methods of the GRS dynamics and platform states used in the data processing are introduced, and the different profiles of the complicate dynamical system that can be drawn from such analysis are reported. We conclude in Sec. 4 with discussions on the applications of such dynamical model to Taiji-1 mission including the ongoing experiments during the extended phase, and how such a framework could be further improved to apply to the planned Taiji-2 mission.

2. Gravitational Reference Sensor Data Analysis

The sensor unit of the electrostatic GRS on-board Taiji-1 is composed of two parts, that the mechanical assembly and the front-end electronics unit (FEE). The mechanical assembly consists of a 72 g parallelepipedic test mass (TM) of titanium alloy and an electrode cage made of ultra low expansion silica that encloses the TM. Both the TM and the cage are gold coated, and inside the cage there are six pairs of electrode facing the TM side faces, see Fig. 2. The TM, which serves as the inertial reference of GRS, is suspended electrostatically inside the cage. When operational, the relative position variations between the TM and the cage (therefore the S/C) cause the variations of the capacitances between the TM side faces and electrodes, which induce signals through Wheatstone bridges and are then picked up by the amplifier of the FEE to give rise to the relative position and attitude data. Based on such position sensor data and the PID algorithm, the TM is servo-controlled to its nominal position inside the cage by applying low frequency actuation voltages through the same electrode in accelerometer mode or by pushing the spacecraft through μN-thrusters in the DFC mode.

The science and housekeeping data are archived and processed at the Taiji-1 data processing center of CAS in Beijing, and the data management and the detailed processing flows can be found in the article "The pipeline of data processing for TAIJI-1 space mission in the TAIJI program for the detection of gravitational wave" from the same issue of this journal. For the GRS system, the level 1 science

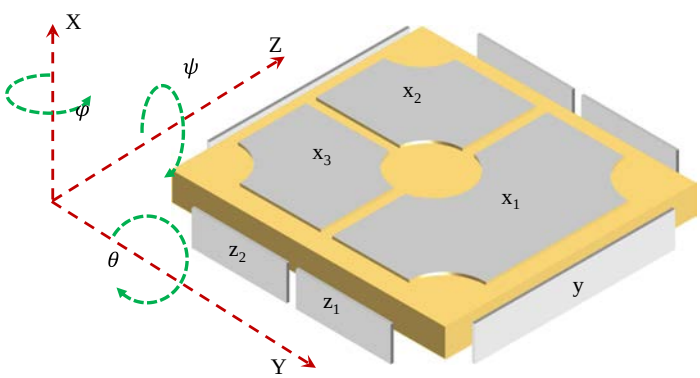

Fig. 2. The geometric structure of the core mechanical assembly of the GRS.

data product contains the actuation voltages on the six electrodes, and with the geometric parameters of the core assembly and the calibrated scale factors and biases, the actuation voltages are transformed into accelerations and angular accelerations data of the TM relative to the cage (see Fig. 2) and then documented as the level 2 science data product. The position sensor data together with the GRS state monitoring data including temperatures of the core assembly and the FEE unit, biased and reference voltages are all packaged as GRS housekeeping data product.

The GRS system is the core payload of Taiji-1, which couples strongly with other instruments or sub-systems on-board such as the laser interferometers, the DFC system and also the satellite platform itself. The scientific objective concerning the GRS is to test the free fall of the inertial reference unit, that the TM suspended inside the electrode cage, in Earth's gravitational field down to the noise floor about $3\times10^{-9}\mathrm{m/s^2/Hz^{1/2}}$@10 mHz. While, in principle, the science measurements of GRS cannot read out directly the motions of the TM relative to the local inertial frame, but can only give the relative motions between the TM and the surrounding cage or the satellite platform. Therefore, since the GRS on-board Taiji-1 is already such a precise instrument, fluctuations of the internal physical environment, such as temperature or magnetic field changes inside the satellite, and mechanical or disturbances of the platform will contribute to main noise terms. To be more specific, the acceleration difference a^i_{ACC} $(i=x,y,z)$ that reflects the dynamics of the TM relative to the satellite platform reads as follows:

$$\begin{aligned} a^i_{\mathrm{ACC}}(t) &= a^i_{\mathrm{TM}}(t) - a^i_{\mathrm{SC}}(t) \\ &= -a^i_{\mathrm{grav,SC}}(t) - a^i_{\mathrm{para,SC}}(t) - a^i_{c,\mathrm{SC}}(t-\tau^i_{\mathrm{DFC}}) \\ &\quad + a^i_{\mathrm{grav,TM}}(t) + a^i_{\mathrm{para,TM}}(t) + a^i_{in,\mathrm{TM}}(t) \\ &= -a^i_{\mathrm{para,SC}}(t) - a^i_{c,\mathrm{SC}}(t-\tau^i_{\mathrm{DFC}}) + a^i_{\mathrm{direc,TM}}(t) + K_{ij}\delta x^j(t) \\ &\quad + T_{ij}(t)\Delta x^j(t) + \omega_{ik}(t)\omega_{kj}(t)\Delta x^j(t) + \dot{\omega}_{ij}(t)\Delta x^j(t) + 2\omega_{ij}(t)\Delta\dot{x}^j(t), \end{aligned} \tag{1}$$

where in the first line, $a^i_{\mathrm{TM}}(t)$ and $a^i_{\mathrm{SC}}(t)$ denote the acceleration of the TM and spacecraft with respect to the local inertial frame. In the second equal, the acceleration difference between the TM and the SC could be expanded, $a^i_{\mathrm{grav,SC}}(t)$ and $a^i_{\mathrm{grav,TM}}(t)$ are the gravitational acceleration of the SC and TM, respectively, and $a^i_{\mathrm{para,SC}}(t)$ and $a^i_{\mathrm{para,TM}}(t)$ are of parasitic accelerations, where $a^i_{\mathrm{para,SC}}(t)$ mainly comes from nonconservative disturbances from solar radiation, air drag and Earth albedo acting on the SC and mechanical disturbances of the SC, and $a^i_{\mathrm{para,TM}}(t)$ are from noise forces acting on the TM including actuation noises, position measurement noises, radiometric effect, contact potential differences, Lorentz forces, magnetic coupling, thermo-noises from gold wire attached to the TM, and etc. $a^i_{c,\mathrm{SC}}(t-\tau^i_{\mathrm{DFC}})$ are accelerations from DFC system having a delay time τ^i_{DFC}, and $a^i_{in,\mathrm{TM}}(t)$ is the inertial acceleration that comes from the attitude variation of the

SC. In the third equal, the difference of the gravitational acceleration of the SC and TM gives rise to the gravitational gradient acceleration that is proportional to the difference between the mass center of the TM and SC Δx, and the last three terms are the inertial accelerations with ω_{ij} the angular velocity of the SC. Parasitic force on TM can be further divided into the direct disturbances $a^i_{\mathrm{direc,TM}}(t)$ and those from the spring-like couplings between the TM and SC.

To evaluate the noise level of the total disturbances of the TMs dynamics with respect to the local reference frame, then $a^i_{\mathrm{para,TM}}(t)$ reads

$$\begin{aligned} a^i_{\mathrm{para,TM}}(t) &= a^i_{\mathrm{direc,TM}}(t) + K_{ij}\delta x^j(t) \\ &= a^i_{\mathrm{ACC}}(t) + a^i_{\mathrm{para,SC}}(t) + a^i_{c,\mathrm{SC}}(t-\tau^i_{\mathrm{DFC}}) \\ &\quad - T_{ij}(t)\Delta x^j(t) - \omega_{ik}(t)\omega_{kj}(t)\Delta x^j(t) - \dot{\omega}_{ij}(t)\Delta x^j(t) - 2\omega_{ij}(t)\Delta\dot{x^j}(t), \\ &= K^0_i + K^1_{ij}a^j_{data}(t) + K^2_i(a^i_{data}(t))^2 + a^i_{\mathrm{para,SC}}(t) + a^i_{c,\mathrm{SC}}(t-\tau^i_{\mathrm{DFC}}) \\ &\quad - T_{ij}(t)\Delta x^j(t) - \omega_{ik}(t)\omega_{kj}(t)\Delta x^j(t) - \dot{\omega}_{ij}(t)\Delta x^j(t) - 2\omega_{ij}(t)\Delta\dot{x^j}(t), \end{aligned} \tag{2}$$

where in the third equal, the acceleration difference is replaced by the GRS measured acceleration data $a^i_{\mathrm{data}}(t)$, and K^0_i, K^1_{ij} and K^2_i denote the bias, scale matrix and the quadratic factor, respectively. To obtain an accurate and delicate evaluation of the noise in the free-fall motions of the TM, one needs to carefully calibrate all the related parameters K^0_i, K^1_{ij}, K^2_i and τ^i_{DFC} of the GRS and the DFC system, and to subtract the modeled disturbances from gravitational gradient, inertial forces, and also mechanical disturbances of the SC. The residuals from the difference of SC perturbations $a^i_{\mathrm{para,SC}}(t)$ and the DFC compensations $a^i_{c,\mathrm{SC}}(t-\tau^i_{\mathrm{DFC}})$ will be a main noise term that limits the precision level of the GRS.

The required experiments concerning GRS planned in the extended phase of the Taiji-1 mission are not all completed yet, especially for those that requiring SC maneuvers are planned in the last phase to reduce risks. Therefore, in the GRS data processing, some of the relevant parameters we used were calibrated with ground-based experiments before the launch. The data will be re-analyzed and the over all performance is expected to be improved after all the experiments are finished. In the following section, we report on the methods we had employed in modeling and subtracting the noises in the last equation from the SC orbit and attitude perturbations, SC mechanical disturbances, and internal environment variations.

3. System Modelings of Taiji-1

3.1. *Orbit dynamics*

As mentioned, the first step is to model the orbit dynamics and attitude dynamics of the spacecraft and the test mass. Together with the observations from the GNSS and star sensor systems, this modeled data are used to remove the gravitational gradients and the inertial force errors.

3.1.1. *Coordinates system*

In the dynamics of spacecraft and test mass, the coordinate systems used include the inertial reference frame, the Earth-fixed reference frame, the orbital reference frame, the satellite fixed reference frame, the test mass's reference frame and the inertial sensor's reference frame. These systems are introduced in what follows.

Inertial reference frame. The inertial reference frame (IRF) is the J2000 equatorial reference system,

$$R_{\mathrm{IRF}} = (O_{\mathrm{IRF}}, X_{\mathrm{IRF}}, Y_{\mathrm{IRF}}, Z_{\mathrm{IRF}}).$$

Its origin O_{IRF} is the Earth's center of mass, the x-axis lies along the intersection between the mean equatorial and ecliptic planes at the epoch J2000.0 (January 1, 2000, 12^h) and points to the vernal equinox, the z-axis is perpendicular to the mean equatorial plane and points from the southern to the north hemisphere, the y-axis completes the right-hand triad.

Earth fixed reference frame. We denote by

$$R_{\mathrm{EFRF}} = (O_{\mathrm{EFRF}}, X_{\mathrm{EFRF}}, Y_{\mathrm{EFRF}}, Z_{\mathrm{EFRF}})$$

the Earth fixed reference frame (EFRF). Its origin O_{EFRF} is the Earth's center of mass, the x-axis lies along the intersection between the mean equatorial and the Greenwich meridian, the z-axis is identical to that of IRF, the y-axis completes the right-hand triad.

Orbital reference frame. We denote by

$$R_{\mathrm{ORF}} = (O_{\mathrm{ORF}}, X_{\mathrm{ORF}}, Y_{\mathrm{ORF}}, Z_{\mathrm{ORF}})$$

the orbital reference frame (ORF). Its origin is the spacecraft's center of mass, the z-axis lies on the line points from the center of mass of spacecraft to that of Earth, the y-axis is perpendicular to the orbital plane and along the direction of the angular momentum, the x-axis completes the right-hand triad.

Satellite fixed reference frame. We denote by

$$R_{\mathrm{SRF}} = (O_{\mathrm{SRF}}, X_{\mathrm{SRF}}, Y_{\mathrm{SRF}}, Z_{\mathrm{SRF}})$$

the satellite fixed reference frame (SRF). Its origin is the spacecraft's center of mass, the x-axis is along the expansion direction of the solar panel, in the Earth orientation mode, it is along the direction of flight, the z-axis is positive towards the nadir of the spacecraft, the y-axis completes the right-hand triad.

Test mass's reference frame. We denote by

$$R_{\mathrm{TMF}} = (O_{\mathrm{TMF}}, X_{\mathrm{TMF}}, Y_{\mathrm{TMF}}, Z_{\mathrm{TMF}})$$

the test mass's reference frame (TMF). Its origin is the center of mass of test mass, its x-axis, y-axis and z-axis are, respectively, identical to the x-axis, y-axis and z-axis of the satellite fixed reference frame.

Inertial sensor's reference frame. We denote by

$$R_{\mathrm{ISF}} = (O_{\mathrm{ISF}}, X_{\mathrm{ISF}}, Y_{\mathrm{ISF}}, Z_{\mathrm{ISF}})$$

the inertial sensor's reference frame (ISF). Its origin is the center of mass of the cage of the inertial sensor, its x-axis, y-axis and z-axis are, respectively, identical to the x-axis, y-axis and z-axis of the satellite fixed reference frame.

3.1.2. *Satellite and test mass dynamics*

(1) Orbit and attitude of spacecraft

In inertial reference frame, the equation of the center of mass of the spacecraft is[14]

$$\ddot{\mathbf{R}}_{\mathrm{SC}}(t) = \mathbf{a}_{\mathrm{grav}} + \mathbf{a}_{d,\mathrm{SC}} + \mathbf{a}_{c.\mathrm{SC}}, \tag{3}$$

where $\mathbf{a}_{\mathrm{grav}}$ is the gravitational acceleration of Earth gravity field, the gravitational force of third bodies, the general relativity correction, $\mathbf{a}_{d,\mathrm{SC}}$ is the nongravitational acceleration, $\mathbf{a}_{c,\mathrm{SC}}$ is the acceleration of the control force. The gravitational force of third bodies contains the direct tides, the indirect tides of third bodies, the ocean tides and the solid Earth pole tides. The nongravitational acceleration consists of the force from air drag, solar radiation pressure and Earth albedo.

Here, the orbit of the spacecraft under the gravitational force from Earth, Sun, Moon and the planets, which consists of Mercury, Venus, Mars, Jupiter, Saturn and Uranus in the solar system, will be simulated. The position vectors of Sun and the planets are provided by JPL's ephemerids DE421.[15] The model of Earth gravity is EGM2008.[16] In the simulation, the orbit data of the Taiji-1 satellite on September 16, 2019 are used as the initial orbit element, such that

$$\begin{aligned} a &= 6067661.398\,m, \\ e &= 0.00154, \\ i &= 97.686183^\circ, \\ \Omega &= 264.400963^\circ, \\ \omega &= 85.732461^\circ, \\ M &= 165.504021^\circ. \end{aligned}$$

The orbit of Taiji-1 is calculated and shown in Fig. 1. Figure 2 shows the distance of Taiji-1 from Earth and the total acceleration generated by Earth, and the direct tides from the third bodies include Sun, Moon and the planets Mercury, Venus, Mars, Jupiter, Saturn and Uranus in the solar system. The total acceleration is about $8\,\mathrm{m/s^2}$ in maximum magnitude. Figure 3 shows the accelerations due to the second-order term in Earth gravity, the all order terms from 3 to 60 and the direct tides from the third bodies. The acceleration due to the second-order term in Earth gravity is about $0.02\,\mathrm{m/s^2}$, the acceleration due to the all order terms from 3 to

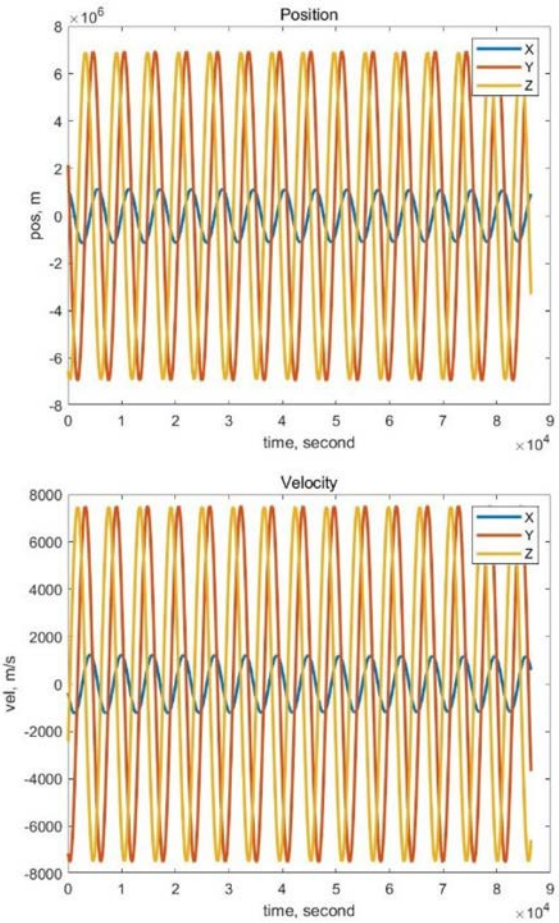

Fig. 3. The orbit of Taiji-1 under the gravitational acceleration of Earth, Sun and other planets in solar system.

60 in Earth gravity is about $3 \times 10^{-4}\,\mathrm{m/s^2}$, and the acceleration due to the direct tides from the third bodies is about $2 \times 10^{-6}\,\mathrm{m/s^2}$.

In the satellite fixed reference frame, the attitude dynamic of the spacecraft is given by

$$\dot{\boldsymbol{\omega}}_{\mathbf{SC}}^{\mathbf{SRF}} = (I_{\mathrm{SC}}^{\mathrm{SRF}})^{-1}[\mathbf{T}_{\mathrm{grav,SC}}^{\mathrm{SRF}} + \mathbf{T}_{d,\mathrm{SC}}^{\mathrm{SRF}} + \mathbf{T}_{c,\mathrm{SC}}^{\mathrm{SRF}} - \boldsymbol{\omega}_{\mathbf{SC}}^{\mathbf{SRF}} \times (I_{\mathrm{SC}}^{\mathrm{SRF}} \boldsymbol{\omega}_{\mathbf{SC}}^{\mathbf{SRF}})], \tag{4}$$

$$\dot{q}_{\mathrm{SC}} = \frac{1}{2}\Omega_{\mathrm{SC}}(\boldsymbol{\omega}_{\mathbf{SC}}^{\mathbf{SRF}})q_{\mathrm{SC}}, \tag{5}$$

where $I_{\mathrm{SC}}^{\mathrm{SRF}}$ is the inertia tensor, $\boldsymbol{\omega}_{\mathbf{SC}}^{\mathbf{SRF}}$ is the angular velocity, q_{SC} is the attitude quaternion, $\mathbf{T}_{\mathrm{grav,SC}}^{\mathrm{SRF}}$, $\mathbf{T}_{d,\mathrm{SC}}^{\mathrm{SRF}}$ and $\mathbf{T}_{c,\mathrm{SC}}^{\mathrm{SRF}}$ are the torques generated by the gravitational force, the nongravitational force and the control force, respectively.

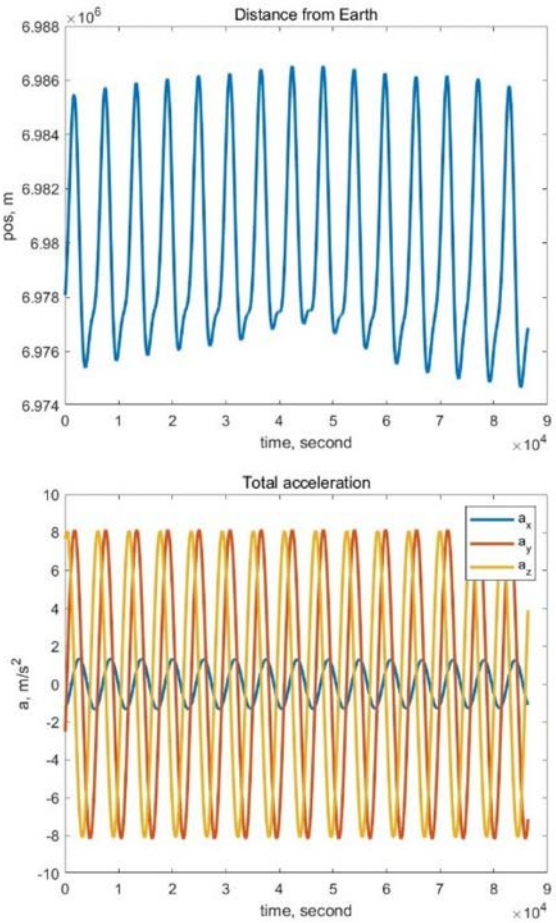

Fig. 4. The distance of Taiji-1 to Earth (up) and the gravitational acceleration of Earth, Sun, Moon and other planets in solar system (below).

The matrix $\Omega_{\rm SC}(\boldsymbol{\omega}_{\mathbf{SC}}^{\mathbf{SRF}})$ is given by

$$\Omega_{\rm SC}(\boldsymbol{\omega}_{\mathbf{SC}}^{\mathbf{SRF}}) = \begin{pmatrix} 0 & \boldsymbol{\omega}_{\mathbf{SC},3}^{\mathbf{SRF}} & -\boldsymbol{\omega}_{\mathbf{SC},2}^{\mathbf{SRF}} & \boldsymbol{\omega}_{\mathbf{SC},1}^{\mathbf{SRF}} \\ -\boldsymbol{\omega}_{\mathbf{SC},3}^{\mathbf{SRF}} & 0 & \boldsymbol{\omega}_{\mathbf{SC},1}^{\mathbf{SRF}} & \boldsymbol{\omega}_{\mathbf{SC},2}^{\mathbf{SRF}} \\ \boldsymbol{\omega}_{\mathbf{SC},2}^{\mathbf{SRF}} & -\boldsymbol{\omega}_{\mathbf{SC},1}^{\mathbf{SRF}} & 0 & \boldsymbol{\omega}_{\mathbf{SC},3}^{\mathbf{SRF}} \\ -\boldsymbol{\omega}_{\mathbf{SC},1}^{\mathbf{SRF}} & -\boldsymbol{\omega}_{\mathbf{SC},2}^{\mathbf{SRF}} & -\boldsymbol{\omega}_{\mathbf{SC},3}^{\mathbf{SRF}} & 0 \end{pmatrix}, \tag{6}$$

where $\omega_{\mathrm{SC},1}^{\mathrm{SRF}}$, $\omega_{\mathrm{SC},2}^{\mathrm{SRF}}$ and $\omega_{\mathrm{SC},3}^{\mathrm{SRF}}$ are the three components of the angular velocity $\boldsymbol{\omega}_{\mathbf{SC}}^{\mathbf{SRF}}$ in the satellite fixed reference frame.

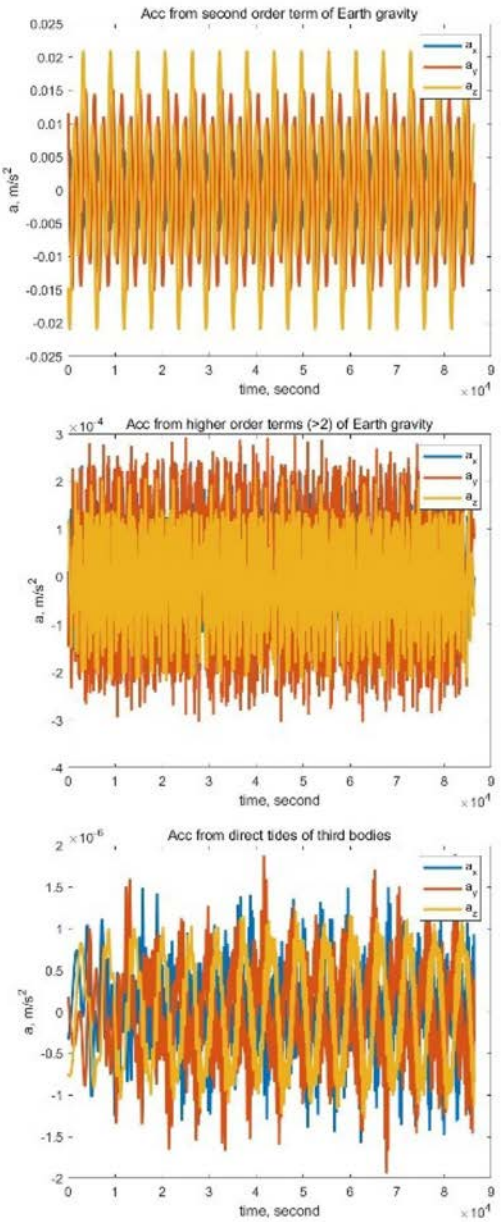

Fig. 5. The acceleration due to the second-order terms of Earth gravitational fields (a), the acceleration due to the all order terms from 3 to 60 of Earth gravity (b) and the direct tide from the third bodies (c).

(2) Test mass's dynamics

In the satellite's fixed reference frame, the equation of motion of the center of mass of the test mass with respect to that of the spacecraft is given by

$$\ddot{\mathbf{r}}_{\mathrm{TM}}^{\mathrm{SRF}}(t) = \Delta\mathbf{g}_{\mathrm{TM}}^{\mathrm{SRF}}(t) + \mathbf{a}_{c,\mathrm{TM}}^{\mathrm{SRF}} + \mathbf{a}_{d,\mathrm{TM}}^{\mathrm{SRF}} + \mathbf{a}_{coup,\mathrm{TM}}^{\mathrm{SRF}} - \mathbf{a}_{c,\mathrm{SC}}^{\mathrm{SRF}} - \mathbf{a}_{d,\mathrm{SC}}^{\mathrm{SRF}} - 2\boldsymbol{\omega}_{\mathbf{SC}}^{\mathbf{SRF}} \times \dot{\mathbf{r}}_{\mathrm{TM}}^{\mathrm{SRF}} - \dot{\boldsymbol{\omega}}_{\mathbf{SC}}^{\mathbf{SRF}} \times \mathbf{r}_{\mathrm{TM}}^{\mathrm{SRF}} - \boldsymbol{\omega}_{\mathbf{SC}}^{\mathrm{SRF}} \times (\boldsymbol{\omega}_{\mathbf{SC}}^{\mathbf{SRF}} \times \mathbf{r}_{\mathrm{TM}}^{\mathrm{SRF}}), \quad (7)$$

where $\mathbf{r}_{\mathrm{TM}}^{\mathrm{SRF}}$ is the relative position vector of test mass with respect to the center of mass of spacecraft, $\Delta\mathbf{g}_{\mathrm{TM}}^{\mathrm{SRF}}(t)$ is the gravitational gravity of test mass with respect to the spacecraft, $\mathbf{a}_{d,\mathrm{TM}}^{\mathrm{SRF}}$ is the nongravitational acceleration of test mass, $\mathbf{a}_{c,\mathrm{TM}}^{\mathrm{SRF}}$ is the acceleration of the control force on test mass, $\mathbf{a}_{coup,\mathrm{TM}}^{\mathrm{SRF}}$ is the coupling acceleration from the spacecraft to the test mass.

In the inertial sensor reference frame, the attitude dynamics of the test mass is given by

$$\dot{\boldsymbol{\omega}}_{\mathbf{TM}}^{\mathbf{ISF}} = -\dot{\boldsymbol{\omega}}_{\mathbf{SC}}^{\mathbf{ISF}} + (I_{\mathrm{TM}}^{\mathrm{ISF}})^{-1}[\mathbf{T}_{\mathrm{grav,TM}}^{\mathrm{ISF}} + \mathbf{T}_{d,\mathrm{TM}}^{\mathrm{ISF}} + \mathbf{T}_{c,\mathrm{TM}}^{\mathrm{ISF}} + \mathbf{T}_{\mathrm{coup,TM}}^{\mathrm{ISF}}] - (I_{\mathrm{TM}}^{\mathrm{ISF}})^{-1}[(\boldsymbol{\omega}_{\mathbf{SC}}^{\mathbf{ISF}} + \boldsymbol{\omega}_{\mathbf{TM}}^{\mathbf{ISF}}) \times (I_{\mathrm{TM}}^{\mathrm{ISF}} \times (\boldsymbol{\omega}_{\mathbf{SC}}^{\mathbf{ISF}} + \boldsymbol{\omega}_{\mathbf{TM}}^{\mathbf{ISF}}))], \quad (8)$$

$$\dot{q}_{\mathrm{TM}} = \frac{1}{2}\Omega_{\mathrm{TM}}(\boldsymbol{\omega}_{\mathbf{TM}}^{\mathbf{ISF}})q_{\mathrm{TM}}, \quad (9)$$

where $I_{\mathrm{TM}}^{\mathrm{ISF}}$ is the inertia tensor of test mass, $\boldsymbol{\omega}_{\mathbf{TM}}^{\mathbf{ISF}}$ is the angular velocity of test mass with respect to the spacecraft, q_{TM} is the attitude quaternion, $\mathbf{T}_{\mathrm{grav,TM}}^{\mathrm{ISF}}$, $\mathbf{T}_{d,\mathrm{TM}}^{\mathrm{ISF}}$, $\mathbf{T}_{c,\mathrm{TM}}^{\mathrm{ISF}}$ and $\mathbf{T}_{\mathrm{coup,TM}}^{\mathrm{ISF}}$ are, respectively, the torques generated by the gravitational force, the nongravitational force, control force and the coupling force from spacecraft. The matrix is given by

$$\Omega_{\mathrm{TM}}(\boldsymbol{\omega}_{\mathbf{TM}}^{\mathbf{ISF}}) = \begin{pmatrix} 0 & \boldsymbol{\omega}_{\mathbf{TM},3}^{\mathbf{ISF}} & -\boldsymbol{\omega}_{\mathbf{TM},2}^{\mathbf{ISF}} & \boldsymbol{\omega}_{\mathbf{TM},1}^{\mathbf{ISF}} \\ -\boldsymbol{\omega}_{\mathbf{TM},3}^{\mathbf{ISF}} & 0 & \boldsymbol{\omega}_{\mathbf{TM},1}^{\mathbf{ISF}} & \boldsymbol{\omega}_{\mathbf{TM},2}^{\mathbf{ISF}} \\ \omega_{\mathbf{TM},2}^{\mathbf{ISF}} & -\boldsymbol{\omega}_{\mathbf{TM},1}^{\mathbf{ISF}} & 0 & \boldsymbol{\omega}_{\mathbf{TM},3}^{\mathbf{ISF}} \\ -\boldsymbol{\omega}_{\mathbf{TM},1}^{\mathbf{ISF}} & -\boldsymbol{\omega}_{\mathbf{TM},2}^{\mathbf{ISF}} & -\boldsymbol{\omega}_{\mathbf{TM},3}^{\mathbf{ISF}} & 0 \end{pmatrix}, \quad (10)$$

where $\omega_{\mathrm{TM},1}^{\mathrm{ISF}}$, $\omega_{\mathrm{TM},2}^{\mathrm{ISF}}$ and $\omega_{\mathrm{TM},3}^{\mathrm{ISF}}$ are the three components of the angular velocity $\boldsymbol{\omega}_{\mathbf{TM}}^{\mathbf{ISF}}$ in the inertial sensor's reference frame.

3.2. *Satellite modal analysis*

3.2.1. *Finite element modelings of Taiji-1 spacecraft*

The main work of modal analysis of the actual structure of Taiji-1 satellite includes the following steps: (1) satellite geometric model's detailed feature processing; (2) structure material database establishment; (3) geometric model finite element mesh generation; (4) element-type selection and contact relationship definition; (5) boundary conditions and simulation conditions; (6) iterative simulation calculation and processing resultant data. Based on finite element modeling, the satellite

launching state constraint condition and the in orbit flight without constraint condition have been analyzed by modal simulation, which provides a design reference for simulation and analysis of the follow-up Taiji missions.

According to the ultra-stable and super-clean design requirements of the Taiji-1 satellite platform, finite element model pre-processing needs to not only manifest the complex structure of Taiji-1 satellite in detail, but also take into account pre-processing workflow clearness and post-processing performance, so as to ensure that the finite element simulation is controllable and accurate. In the aspect of material parameter modeling, more than 10 classes of general material libraries are established, which include aluminum alloy material, aluminum honeycomb plate material for satellite main structure, titanium alloy materials for core platform, polyimide insulation gasket, FRP gasket material for structural connection, invar material for optical platform base, gold wire material, payload control box material, solar substrate, etc. Equal-sized grid is used in each component partitions. At the same time, the grid size and the number of units of different components are comprehensively adjusted. For example, the grid size of the inertial sensor and optical platform equipment is small, and the number of units is large; the satellite solar cell substrate configuration is regular and its grid size is slightly bigger, and the number of units is less. The grid division of Taiji-1 satellite is shown in Figs. 6 and 7. The model is divided into 949,300 units with 2,075,176 nodes in total.

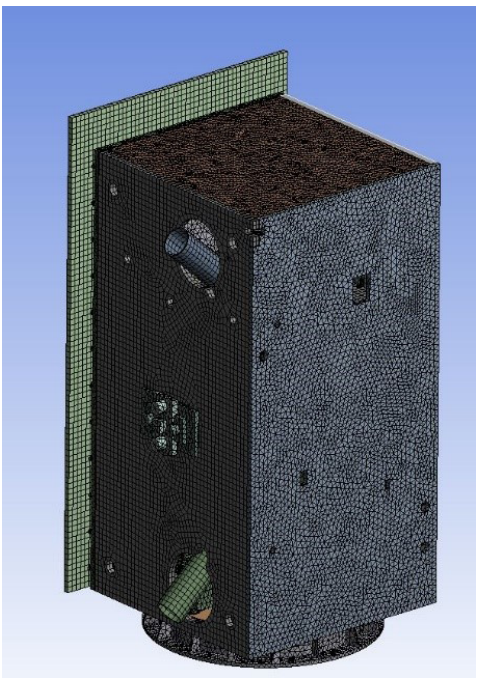

Fig. 6. Grid element division of Taiji-1 satellite.

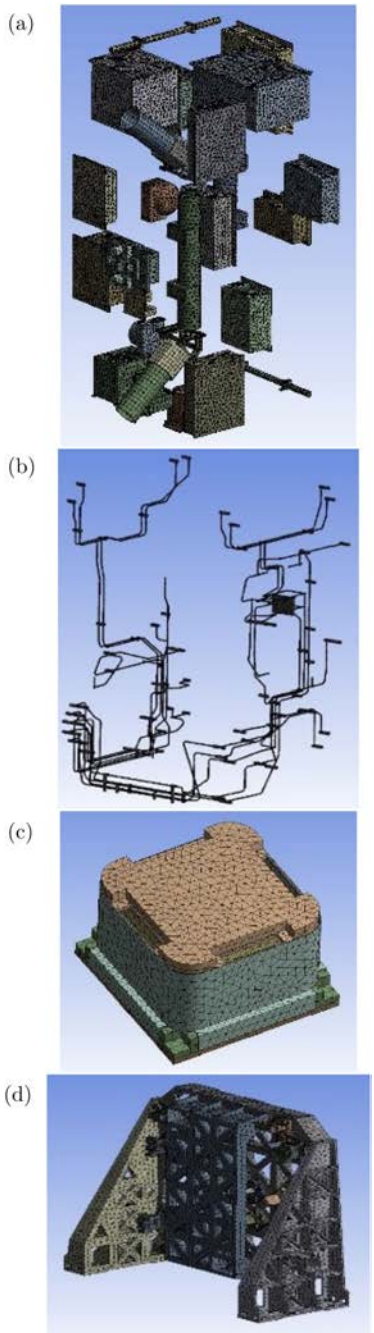

Fig. 7. Grid generations of onboard equipment (a), cold air pipeline (b), GRS (c) and optical platform (d).

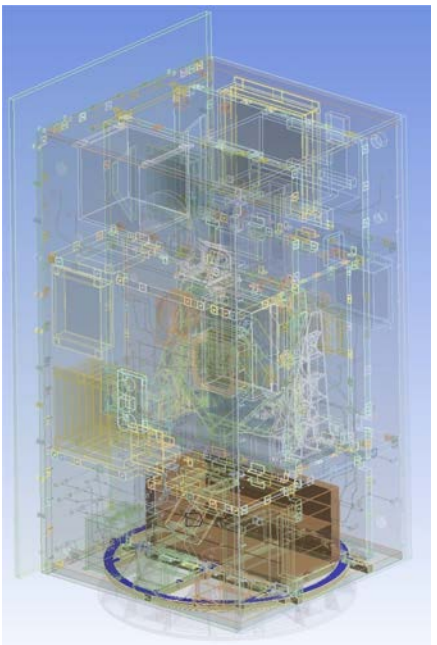

Fig. 8. Contact pairs of components.

In the connection modelings, a lot of position correction work has been done, and the numerical setting of contact tolerance of diagonal piece and glass fiber reinforced plastic gasket is optimized iteratively. Finally, the tolerance value of 0.01 mm is determined, with 1256 contact pairs established in total, and the consistency between the finite element model and the actual components of the satellite is realized, as shown in Fig. 8.

The irregular configuration of small and light components has little effect on the dynamic characteristics of the whole satellite. Therefore, it is not suitable to use it as a solid model for mesh generation which will increase the amount of simulation calculation. For example, micro equipment such as TT & C transmitting antenna, GNSS antenna, various solenoid valves of air-conditioning pipeline can be directly attach to the model element node at its corresponding position as mass points. The equivalent concentrated mass point model of Taiji-1 satellite is shown in Fig. 9.

3.2.2. *Modal simulation analysis with the launching state constraint condition*

According to the fixed installation constraints of the Taiji-1 satellite actual launching structure, six degrees of freedom of the mechanical installation hole unit node at the bottom of the docking ring are constrained, and the structural modal simulation calculation is carried out. Results showed that the fundamental frequency (first-order mode) of the whole satellite structure is 18.836 Hz, and the corresponding

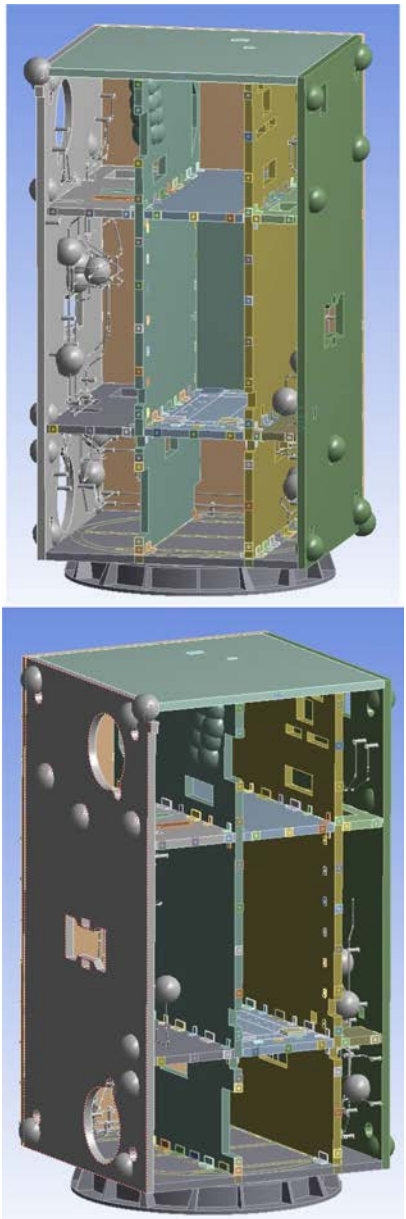

Fig. 9. Equivalent lumped mass point model of Taiji-1 satellite.

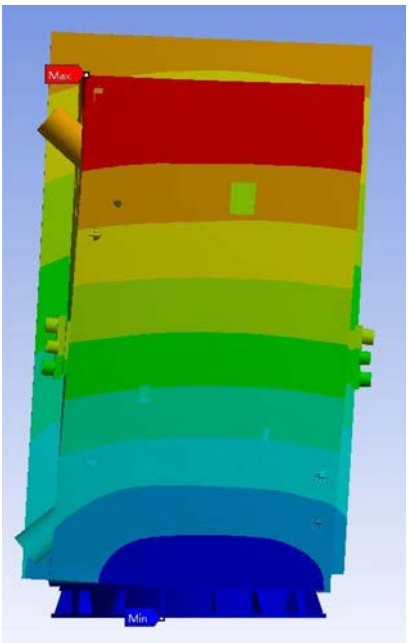

Fig. 10. The first-order mode shape of the whole satellite launching state.

modal vibration mode is the vibration of the whole satellite around the docking ring plane 2-dimensional coordinate axis, as shown in Fig. 10.

3.2.3. *Free mode simulation and analysis*

Structural free mode simulation calculation is carried out directly for the whole satellite finite element model under the condition of no external constraint conditions. The simulation results of the first six main modal frequencies and structural vibration modes except for the whole satellite rigid body free modes are shown in Table 1.

Table 1. The first six main modal frequencies and structural vibration modes of rigid body free modes except the whole satellite.

Modal order	Modal frequency (Hz)
1	40.367
2	50.997
3	55.173
4	60.527
5	72.93
6	76.917

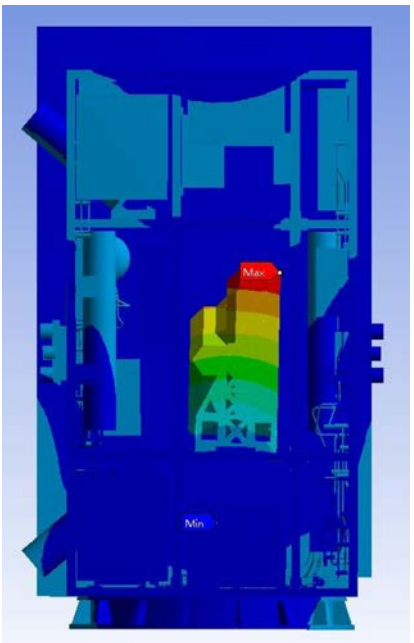

Fig. 11. Mode shapes of the third-order free mode integral core measurement platform of the whole satellite.

Among them, the third mode vibration mode is the whole core measuring platform's vibration, which is around the long side axis of its fixed installation surface (as shown in Fig. 11). The modal frequency is 55.173 Hz. The whole core measurement platform contains the inertial sensor, optical measurement platform and other core components, which is one of the key scientific payloads of Taiji-1 satellite. The simulated results showed that if the fixed installation position of the whole core measurement platform is disturbed by external interference force with the frequency of 55.173 Hz or its nearby frequency value, its structure will resonate or vibrate greatly and cause great error to the vibration displacement detection of the test masses.

3.3. *Temperature fluctuations and GRS bias drifts*

In the normal measurement mode, the gravitational reference sensor gives out the displacements and accelerations measurement data of six channels $X1$, $X2$, $X3$, Y, $Z1$ and $Z2$, which change with the nonconservative forces acted on the SC, and are also affected by drifts of the scale factors and biases of the inertial sensor. The nonconservative force acted on the SC is dominated by the atmospheric drag, solar radiation pressure, and earth albedo, which depends on the orbit position and attitude of the satellite. The bias of the gravitational reference sensor FEE is mainly caused by the parasitic forces acted on the test mass, and also the asymmetry of

sensor electrode geometry and FEE circuit in certain axis. The temperature fluctuation of gravitational reference sensor FEE circuit will also lead to the fluctuation of inertial sensor readouts.

Temperature sensors were installed across the satellite platform to measure the temperature fluctuations near the key scientific payload, among which Nos. 45 and 46 temperature sensors attached on the inertial sensor FEE cabinet are used to monitor the temperature fluctuation of the gravitational reference sensor FEE. To qualitatively study the influence of FEE temperature fluctuation on the readouts of gravitational reference sensor, we analyze the correlations between the 6 channel readouts of gravitational reference sensor and the temperature sensors.

From November 8 to 15, 2019, Taiji-1 conducted inertial sensor FEE temperature influences experiment. We selected 21 sets of data from different time periods, as shown in Fig. 12, to study how FEE temperature affects gravitational reference sensor readouts. Each set of data is 10 min long and is taken as the average. Figure 13 compares between mean actuation voltage of inertial sensor channels and

	time	temperature of No.45(°C)	Temperature of No.46(°C)	x1-ACC(V)	x2-ACC (V)	x3-ACC (V)	y-ACC (V)	z1-ACC (V)	z2-ACC (V)
1	20191108T22:08	1.85	6.04	0.14225	0.0294	0.148	-0.07278	-0.07567	0.04731
2	20191109T00:55	18.19	26.38	0.1446	0.03198	0.14968	-0.07018	-0.07279	0.04964
3	20191109T08:13	19.96	27.93	0.14474	0.03215	0.1498	-0.06997	-0.07251	0.04982
4	20191109T13:45	20.03	27.97	0.14473	0.03216	0.14977	-0.06994	-0.07253	0.04985
5	20191109T17:59	20	28.08	0.1447	0.03208	0.14977	-0.06996	-0.07246	0.049
6	20191109T23:54	20.04	28.36	0.14472	0.03215	0.14974	-0.0689	-0.07245	0.04992
7	20191110T06:35	20.01	28.16	0.14468	0.03212	0.14975	-0.0699	-0.07247	0.04987
8	20191110T10:46	20	28.04	0.14465	0.03211	0.14969	-0.06993	-0.07246	0.04983
9	20191111T00:06	20.06	28.4	0.14466	0.0321	0.1497	-0.06987	-0.07234	0.0499
10	20191111T05:57	19.99	28	0.14461	0.03205	0.14968	-0.06991	-0.07247	0.04983
11	20191111T09:14	19.95	27.93	0.1446	0.03204	0.14966	-0.06992	-0.07247	0.04981
12	20191111T09:14	20.03	28.37	0.14462	0.03207	0.14966	-0.06984	-0.07242	0.04993
13	20191112T04:31	19.98	27.94	0.14458	0.03203	0.14966	-0.06987	-0.07245	0.04984
14	20191112T07:53	20.04	28.06	0.14458	0.03204	0.14964	-0.06986	-0.0724	0.04982
15	20191112T22:52	20.08	28.45	0.14459	0.03204	0.14964	-0.0698	-0.07231	0.0499
16	20191113T04:43	19.96	27.91	0.14454	0.032	0.14963	-0.06985	-0.07243	0.04984
17	20191113T08:05	20.06	28.09	0.14455	0.03203	0.1496	-0.06984	-0.07235	0.0498
18	20191113T23:01	20.03	28.37	0.14457	0.03204	0.14963	-0.06977	-0.07233	0.04991
19	20191114T08:15	20	27.99	0.14451	0.03198	0.14958	-0.06982	-0.07233	0.04981
20	20191114T23:09	20	28.29	0.14453	0.03201	0.14959	-0.06976	-0.07225	0.04988
21	20191115T08:29	20.02	28.04	0.1445	0.032	0.14958	-0.06978	-0.07237	0.04981

Fig. 12. Inertial sensor FEE temperature influence experiments.

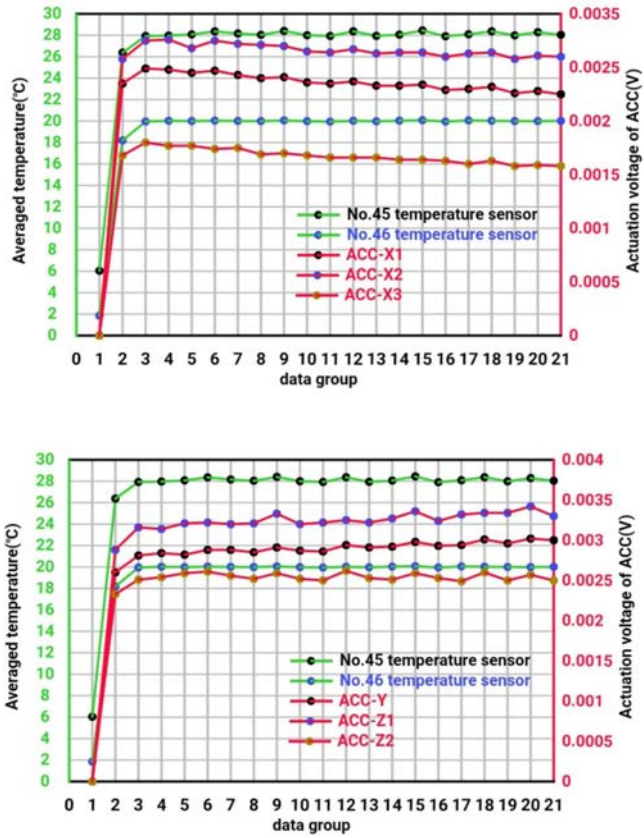

Fig. 13. Comparison between mean actuation voltage of inertial sensor channels and mean value of temperature sensors.

mean value of temperature sensors. The abscissa of these figures is serial number of 21 groups of data, the left ordinate is temperature ranges of the temperature sensor, the right ordinate is actuation voltage ranges of gravitational reference sensor electrode, the green curve shows average temperature change of the temperature sensor, the brown curve represents average actuation voltage fluctuation of the gravitational reference sensor electrodes. It is obvious that there are high correlations between the average actuation voltages of each gravitational reference sensor electrode and the average temperatures of sensor.

According to the statistical analysis of temperatures near the gravitational reference sensor FEE and actuation voltages of each gravitational reference sensor channel, the temperature sensor near the inertial sensor FEE reaches a relative equilibrium temperature about 12 h after the inertial sensor is turned on, and then its temperature goes up and down near the temperature equilibrium point. Actuation voltages of the gravitational reference sensor change monotonously with the temperature fluctuation of the FEE.

Table 2. The correlation coefficients between the averaged actuation voltages of each channel and FEE temperature measurements.

	$r(T, X1)$	$r(T, X2)$	$r(T, X3)$	$r(T, Y)$	$r(T, Z1)$	$r(T, Z2)$
Sensor A	0.9876	0.9946	0.9802	0.9961	0.9957	0.9986
Sensor B	0.9861	0.9937	0.9792	0.9958	0.9952	0.9970

Table 3. The linear fittings between actuations and the temperature measurements.

	$X1$	$X2$	$X3$	Y	$Z1$	$Z2$
Sensor A	0.00011	0.00012	0.00008	0.00013	0.00015	0.00012
Sensor B	0.00013	0.00015	0.00009	0.00016	0.00018	0.00014

Table 2 shows the correlation coefficients between the averaged actuation voltages of each gravitational reference sensor channel and the average temperatures of the temperature sensors attached on the electronic box. There is a correlation of more than 0.98 for the No. 46 temperature sensor, and a correlation of more than 0.979 for the No. 45 temperature sensor. These results show that the change of electronic temperature is the main factor causing the drifts of the measurement output of the inertial sensor.

In order to quantitatively analyze the influence of FEE temperature fluctuation on the actuation voltages of the inertial sensor, linear fitting analysis is adopted on the temperature of Nos. 45 and 46 temperature sensor and the actuation voltages of each gravitational reference sensor channel. The fitting results are shown in Table 3.

When the temperature of the No. 46 temperature sensor changed by 1 K, the actuation voltages of the gravitational reference sensor changed correspondingly by 80–150 ppm. For No. 45 temperature sensor, the actuation voltages changed by 90–180 ppm. Consider that the temperatures of Nos. 45 and 46 temperature sensors are lower than the FEE temperature, between which there exists a temperature gradient, it can be inferred that the temperature fluctuation of 1 K in the gravitational reference sensor FEE will cause about 100 ppm actuation voltage fluctuation of each gravitational reference sensor channel.

4. Conclusions

Based on the GRS data analysis framework, Eqs. (1) and (2), introduced in Sec. 2, three main noise sources in the GRS measurement from SC dynamical perturbations, platform disturbances and temperature fluctuations near the GRS system inside the satellite are carefully modeled and analyzed in Sec. 3.

The SC orbit perturbations from Earth geopotentials and nonconservative forces are very useful reference data for the extended experiments to measure the global gravitational field. The amplitude spectrum density of the perturbations from nonconservative forces is compared directly with the GRS science data, their consistency provides the preliminary validation of the status and performance of the

GRS payload and satellite platform. The SC attitude perturbations are measured by on-board star sensors, and, based on Eq. (2), the inertial accelerations exerted by the TM due to the possible mass center difference between TM and SC are smoothed and carefully subtracted from the GRS science data. At this stage, only low frequency components of the inertial accelerations are corrected in the data processing since the precision of the SC attitude data is not good enough in high frequency band near 1 Hz. In future work, after the more complete calibrations of the GRS and DFC systems, the data of star sensors and angular acceleration data from GRS should be combined to give rise to a full band corrections of the inertial accelerations. The disturbances of the satellite platform are modeled with finite-element method. The vibration modes of the platform are of higher frequencies > 40 Hz. But, still, some peaks in the ASD of the GRS science data can be identified as been produced by aliasing effect during the on-board sampling procedure when high frequency disturbances exist. This leads to the upload of the updated anti-aliasing filter to the on-board data processing unit. For the SC internal environment fluctuations, the magnetic field variations and the TM perturbations from magnetic torque and Lorentz forces are still under investigation. The clear correlations between temperature changes and GRS actuation bias drifts are detected. The linearly correlation coefficients are fitted out through the designed in-orbit experiments, which are applied to subsequent GRS data processing.

The system modeling and GRS data analysis framework reported in this work are still under development. For the ongoing experiments in Taiji-1's extended phase, a much more complicated and completed modeling and processing framework are about to be established. This work lays the theoretical foundations and plays a key role in understanding and processing the complicated data of the multi-coupled and highly accurate GRS system of Taiji-1 mission. Based on these preliminary studies, the R&D of the modeling and processing system designed for Taiji-2 mission had been commissioned this year.

Acknowledgments

This work has been made possible by the Taiji-1 mission, which is the pre-PathFinder mission of the Taiji Program in Space conducted by CAS. The Strategic Priority Research Program of the Chinese Academy of Sciences Grant XDA15020700, Nos. XDA1502070401, XDA1502070801 and XDA1502070903-01 are acknowledged. This work is also supported by the State Key Laboratory of applied optics, Changchun Institute of Optics, Fine Mechanics and Physics, Chinese Academy of Sciences. The first and second author equally contribute to this work.

References

1. B. P. Abbott *et al.*, *Phys. Rev. Lett.* **116**, 131103 (2016).
2. B. P. Abbott *et al.*, *Phys. Rev. Lett.* **116**, 241102 (2016).
3. W. Hu and Y. Wu, *Nat. Sci. Rev.* **4**, 685 (2017).

4. Z. Luo *et al.*, *Res. Phys.* **16**, 102918 (2020).
5. Z. Luo *et al.*, *Prog. Theor. Exp. Phys.* 083 (2020).
6. X. Gong *et al.*, *Class. Quantum Grav.* **28**, 094012 (2011).
7. Z. Luo *et al.*, *Adv. Mech.* **43**, 415 (2013).
8. X. Gong *et al.*, *J. Phys. Conf. Ser.* **610**, 012011 (2015).
9. X. Gong *et al.*, *Chin. Astron. Astrophys.* **39**, 411 (2015).
10. D. Blair *et al.*, *Sci. China Phys. Mech. Astron.* **58**, 120402 (2015).
11. W. Gao *et al.*, *Sci. China Phys. Mech. Astron.* **58**, 014201 (2015).
12. W. Ruan *et al.*, *Nat. Astron.* **4**, 108 (2020).
13. The Taiji Scientific Collaboration, *Commun. Phys.* **4**, 34 (2021).
14. O. Montenbruck and E. Gill, *Appl. Mech. Rev.* **55**(2), B27–B28 (2002).
15. W. M. Folkner *et al.*, *IPN Prog. Rep.* **42-178**, 1 (2009).
16. N. M. Pavlis *et al.*, *J. Geophys. Res. Solid Earth* **117**, B04406 (2013).